PHYSICS OF FLUIDS **26**, 072105 (2014)

Free surface due to a flow driven by a rotating disk inside a vertical cylindrical tank: Axisymmetric configuration

L. Kahouadji[a] and L. Martin Witkowski
UPMC, 4 place Jussieu, F-75005 Paris, France and CNRS, UPR 3251, LIMSI, F-91403 Orsay, France

(Received 9 December 2013; accepted 27 June 2014; published online 28 July 2014)

The flow driven by a rotating disk at the bottom of an open fixed cylindrical cavity is studied numerically and experimentally. The steady axisymmetric Navier-Stokes equations projected onto a curvilinear coordinate system are solved by a Newton-Raphson algorithm. The free surface shape is computed by an iterative process in order to satisfy a zero normal stress balance at the interface. In previous studies, regarding the free surface deflection, there is a significant disagreement between a first-order approximation [M. Piva and E. Meiburg, "Steady axisymmetric flow in an open cylindrical container with a partially rotating bottom wall," Phys. Fluids **17**, 063603 (2005)] and a full numerical simulation [R. Bouffanais and D. Lo Jacono, "Unsteady transitional swirling flow in the presence of a moving free surface," Phys. Fluids **21**, 064107 (2009)]. For a small deflection, the first-order approximation matches with our numerical simulation and for a large deflection a good agreement is found with experimental measurements. © *2014 AIP Publishing LLC*. [http://dx.doi.org/10.1063/1.4890209]

I. INTRODUCTION

There has been much interest in understanding flows inside an open and fixed vertical cylindrical tank, driven by the rotation of the bottom when the top is a free surface. Such flows have often been studied in the two distinct situations of *flat* or *deformable* free surface.

In the first situation, for a given cavity radius and gravitational acceleration, very weak rotation of the bottom leads to a very small free surface deflection. The denomination of *flat free surface* often used in numerical studies is a convenient shortcut to refer to the limit case where the geometry of the free surface is fixed at a constant height and a stress-free boundary condition is imposed. This configuration has been very popular since the first visualizations of Spohn *et al.*,[1–3] because it develops an intriguing variety of secondary toroidal circulation mechanisms, which are formed even under steady, laminar, and axisymmetric conditions. From this first series of flow visualizations, Spohn *et al.*[1–3] reported that the secondary circulation could be located along the rotating axis, such as was already observed in the case of an enclosed cavity, otherwise it also could appear at the free surface. Assuming a flat interface, Daube[4] was the first to carry out a two-dimensional and axisymmetric time-dependent simulation in order to reproduce Spohn's experiments (Spohn and Daube[1]), emphasizing that there are situations in which secondary circulations with very low circulation are detected numerically but could not be experimentally observed. Brøns *et al.*[5] conducted both numerical and theoretical studies in order to detect the appearance of secondary circulation and compared it to the experiments of Spohn *et al.*[1–3] Their theoretical study consists in studying the steady solution of vorticity-stream function formulation as a Hamiltonian dynamical system. Piva and Meiburg[6] performed a simulation in which the bottom disk partially rotates. However, they also gave a very clean experimental observation of a situation in which the entire bottom rotates

[a]Electronic mail: lyes.kahouadji@univ-lehavre.fr. Present address: Laboratoire Ondes et Milieux Complexes, UMR 6294, CNRS-Université du Havre, 76058 Le Havre Cedex, France.

and gives rise to a secondary circulation detached from the axis. Serre and Bontoux[7] performed a three-dimensional Navier-Stokes simulation, in which the fluid height is four times the cavity radius, highlighting that the instability thresholds are 15% lower than those of an enclosed cavity. Poncet and Chauve[8] experimentally investigated cavities with very small aspect ratios (height/radius <0.107) for which two distinct regions are observed. The first, close to the axis, rotates as a solid body and the other region, near the fixed side wall, behaves almost as a shear flow in which polygonal patterns are observed in the azimuthal direction.

When the disk rotation is strong, the free surface cannot be taken as flat. Moreover, if the fluid is very viscous, the flow remains steady and laminar even under large free surface deflection. To our knowledge, the first study analyzing the free surface deformation is the experiment of Vatistas[9] with the specificity that the bottom disk partially rotates. He observed that, for different parameters linked to the aspect ratio and the disk's angular velocity, the free surface deflection takes the shape of an inverted bell. By increasing the angular velocity beyond a critical value, the free surface touches the rotating disk and dries it periodically in its azimuthal direction which leads to polygonal patterns. Thereafter, Vatistas *et al.*[10] carried out experiments in a range of parameters so as to exceed a sloshing state where the free surface just reaches the rotating disk. He provided a stability diagram showing the azimuthal wave numbers as a function of the fluid height and the disk's angular velocity. With the exception of several studies described in the previous paragraph, the deformable free surfaces were not pursued further in depth. It was 14 years later that simultaneously Suzuki *et al.*[11] and Jansson *et al.*[12] reported on this topic. Suzuki *et al.*[11] studied a cavity whose aspect ratio is 0.94, for which they measured the free surface height at the z-axis as a function of the Reynolds number Re (the Reynolds number is defined in Sec. II B). Four states were detected for increasing Re:

1. The first state, which is axisymmetric and steady, appears for Re between 0 and 1.31×10^5. The fluid height at the z-axis decreases monotonically as a function of Re. It is also the state which Vatistas[9] described as an inverted bell.
2. The second state, called switching, appears when Re varies between 1.31×10^5 and 1.58×10^5. The free surface reaches the rotating disk at the axis by drying it from its center $r \sim 0$. This switching state corresponds to the sloshing state described 16 years earlier by Vatistas.[9]
3. The third state mentioned is asymmetric and appears by increasing Re between 1.58×10^5 and 2.37×10^5. The free surface develops two rotating concave surfaces.
4. Finally, the last state regains symmetry, appearing when Re is larger than 2.37×10^5 and develops by the fusion of the two previous concavities forming a single axisymmetric concavity.

In the same year, Jansson *et al.*[12] carried out experiments for which the free surface is strongly deformed and dries the rotating disk resulting in intriguing polygonal forms. Two years later, Abderrahmane *et al.*[13] further investigated the experiments of Vatistas[9,10] for which they deduced a relationship between the rotating disk frequency and the different azimuthal modes obtained. In the same year, Tasaka and Iima[14] further pursued the studies of Suzuki *et al.*,[11] highlighting hysteresis for the free surface deformation as a function of Re. Beyond the four states developed by Suzuki *et al.*,[11] it is possible to combine the four states into two stages, which consist of a stage of symmetry breaking and then its reconstruction. The experimental work on polygonal forms by Jansson *et al.*[12] has been extended by Bergmann *et al.*[15] and the theoretical study of Tophøj *et al.*[16] provides an interpretation of the rotating polygon instability in terms of a coupling between surface waves. Bouffanais and Jacono[17] carried out the first numerical study which takes into account the free surface deformation. They used a spectral method with Lagrange-Legendre polynomial approximation. However, their calculations are limited to a very small free surface deflection. Brady *et al.*[18,19] numerically simulated two-fluid confined flow in a cylinder driven by a rotating end wall. However, even if the interface deflection is large, the densities of the two fluids are very close. Recently, the configuration with large free surface deformation and large density ratio between the two fluids has been tackled numerically by Herrada *et al.*[20] In their study, the surface tension effects are large as the radius of the disk is chosen very small (1 mm) which is difficult to achieve experimentally. A numerical computation directly related to an experimental facility was still missing.

This article is organized into four sections. After this introductory part, in which we summarized past studies, Sec. II sets the governing equations, the computational methods, and then describes

the way in which the free surface profile is obtained. Section III presents results on both flat and deformable interfaces. Experimental measurements are also provided in order to validate this study. Finally, we present our conclusions followed by future work that will be interesting to pursue.

II. PROBLEM FORMULATION, GOVERNING EQUATIONS, FREE SURFACE COMPUTATION, AND FLOW DESCRIPTION

A. Problem formulation

The experimental setup is shown in Fig. 1. Cylindrical coordinates (r^*, θ^*, z^*) are used, where asterisks indicate dimensional variables. A disk of radius R^* rotates at an angular velocity Ω^* located at the bottom of an open vertical cylindrical cavity with an inner radius also R^*. The fluid enclosed inside this tank is assumed to be incompressible and Newtonian with uniform density ρ^* and kinematic viscosity ν^*. The liquid height above the rotating disk at rest is H^*.

B. Equations of motion and computational methods

To nondimensionalize the equations, the characteristic scales selected are the disk radius R^* for the length and $1/\Omega^*$ for the time. The velocity and pressure are then, respectively, scaled by $\Omega^* R^*$ and $\rho(\Omega^* R^*)^2$. The base flow, before reaching the first bifurcation, is described by the stationary axisymmetric Navier-Stokes equations with velocity $\mathbf{U} = (U_r, U_\theta, U_z)^t$. We write the equations using the stream-function ψ, vorticity ω, and angular momentum Γ. This is achieved by the introduction of a stream-function ψ

$$U_r = \frac{1}{r}\frac{\partial \psi}{\partial z} \ , \ U_z = -\frac{1}{r}\frac{\partial \psi}{\partial r}, \tag{1}$$

which satisfies continuity and gives for the azimuthal component of vorticity and angular momentum

$$\omega = \frac{\partial U_r}{\partial z} - \frac{\partial U_z}{\partial r} \text{ and } \Gamma = r U_\theta. \tag{2}$$

Incorporating (1) and (2) in the stationary and axisymmetric Navier-Stokes equations leads to the following equations of motion:

$$\frac{\partial}{\partial r}\left(\frac{1}{r}\frac{\partial \psi}{\partial z}\omega\right) - \frac{\partial}{\partial z}\left(\frac{1}{r}\frac{\partial \psi}{\partial r}\omega\right) - \frac{\partial}{\partial z}\left(\frac{\Gamma^2}{r^3}\right) = \frac{1}{Re}\left(\frac{\partial^2 \omega}{\partial r^2} + \frac{1}{r}\frac{\partial \omega}{\partial r} - \frac{\omega}{r^2} + \frac{\partial^2 \omega}{\partial z^2}\right), \tag{3}$$

$$\frac{\partial^2 \psi}{\partial r^2} - \frac{1}{r}\frac{\partial \psi}{\partial r} + \frac{\partial^2 \psi}{\partial z^2} = r\omega, \tag{4}$$

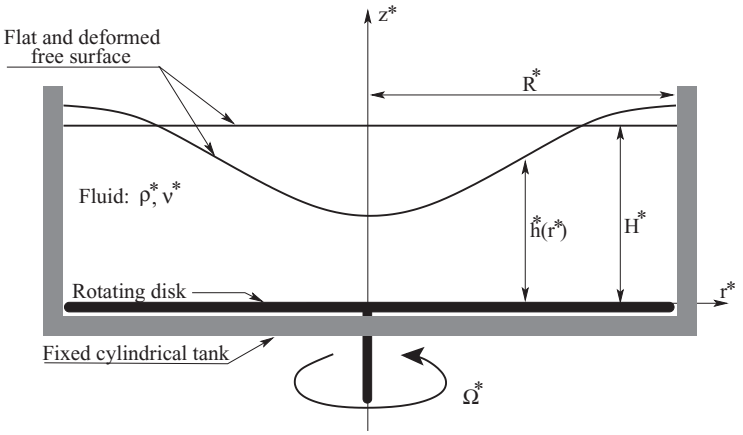

FIG. 1. Sketch of the experiment.

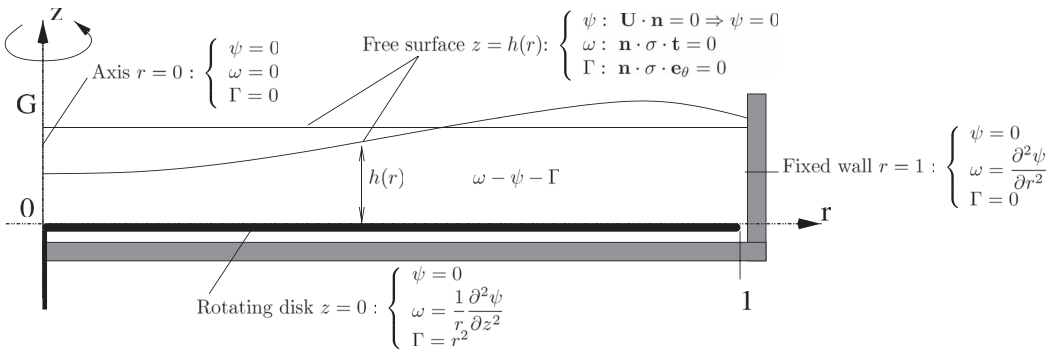

FIG. 2. The theoretical non-dimensional configuration with its boundary conditions.

$$\frac{\partial}{\partial r}\left(\frac{\partial\psi}{\partial z}\Gamma\right)-\frac{\partial}{\partial z}\left(\frac{\partial\psi}{\partial r}\Gamma\right)=\frac{r}{Re}\left(\frac{\partial^2\Gamma}{\partial r^2}-\frac{1}{r}\frac{\partial\Gamma}{\partial r}+\frac{\partial^2\Gamma}{\partial z^2}\right). \tag{5}$$

The Reynolds number is defined by $Re=\Omega^* R^{*2}/\nu$ and appears in the diffusive terms of (3) and (5). The aspect ratio $G=H^*/R^*$ is the second non-dimensional parameter for this problem (see Fig. 2). In order to complete the system of equations (3), (4), and (5), the velocity is required to satisfy the impermeability condition on both the rotating disk ($z=0$) and the fixed sidewall ($r=1$). Moreover, a regularity condition is applied at the z-axis ($r=0$). The boundary conditions relevant to the rotating disk, the axis and the fixed vertical side wall are

$$\begin{cases} z=0\ :\ \psi=0\,,\ \omega=\dfrac{1}{r}\dfrac{\partial^2\psi}{\partial z^2}\ \text{ and }\ \Gamma=r^2, \\ r=0\ :\ \psi=0\,,\ \omega=0\ \text{ and }\ \Gamma=0, \\ r=1\ :\ \psi=0\,,\ \omega=\dfrac{\partial^2\psi}{\partial r^2}\ \text{ and }\ \Gamma=0. \end{cases} \tag{6}$$

Furthermore, the velocity field must be tangent to the free surface under the constraint of a zero shear. The surface tension and the air motion are both neglected. The boundary conditions at the free surface $z=h(r)$ are then

$$\begin{cases} \mathbf{U}\cdot\mathbf{n}=0\Rightarrow U_z=h'(r).U_r\Longrightarrow\psi=0, \\ \mathbf{t}\cdot\underline{\underline{\mathcal{D}}}\cdot\mathbf{n}=0\Rightarrow r\omega=\dfrac{2}{(h'^2+1)}\left(\dfrac{\partial^2\psi}{\partial r^2}+2h'\dfrac{\partial^2\psi}{\partial r\partial z}+h'^2\dfrac{\partial^2\psi}{\partial z^2}\right), \\ \mathbf{e}_\theta\cdot\underline{\underline{\mathcal{D}}}\cdot\mathbf{n}=0\Rightarrow -h'\left(\dfrac{\partial\Gamma}{\partial r}-\dfrac{2\Gamma}{r}\right)+\dfrac{\partial\Gamma}{\partial z}=0, \end{cases} \tag{7}$$

where $\underline{\underline{\mathcal{D}}}$, h', $\mathbf{n}=\frac{1}{\sqrt{h'^2+1}}(-h',0,1)^t$ and $\mathbf{t}=\frac{1}{\sqrt{h'^2+1}}(1,0,h')^t$ are the deformation tensor, the free surface slope, and the normal and tangent vectors, respectively. We have already indicated that with a slow rotating disk, the liquid height can be approximated as constant (flat free surface). However, for large angular velocity Ω^*, it is no longer realistic to impose the flatness of the free surface. The r-z plane becomes a surface ($(r,z)\in[0,1]\times[0,h(r)]$). We introduce a curvilinear coordinate system for which each point of the r-z plane is defined by new curvilinear coordinates

$$\Big(r,z\Big)\longrightarrow\Big(\xi(r,z),\eta(r,z)\Big) \tag{8}$$

and for which the boundaries ($r=0$ or 1 and $z=0$ or $h(r)$) will correspond to one of the surfaces $\xi=$ constant or $\eta=$ constant. This leads us to define a projection formula from cylindrical to curvilinear

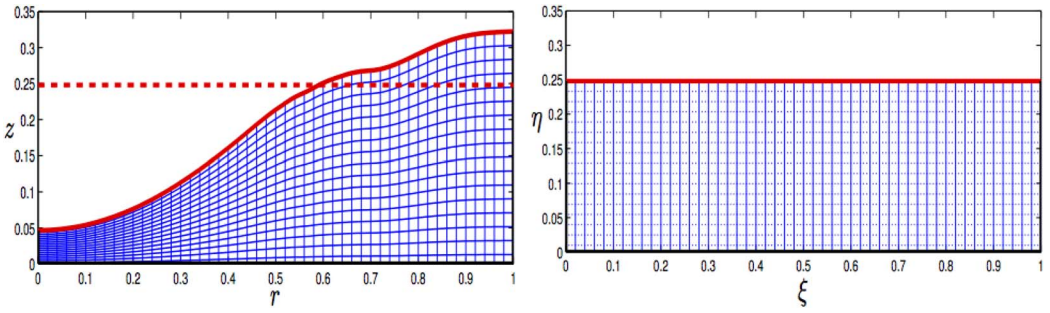

FIG. 3. Physical (left) and curvilinear (right) meshing used for the discretization.

coordinates by

$$\xi = r \ \text{ and } \ \eta = \frac{G}{h} z. \tag{9}$$

Fig. 3 illustrates the curvilinear projection used in (9) and shows the way that an irregular domain, $(r, z) \in [0, 1] \times [0, h(r)]$ as shown in Fig. 3(left), is simplified to a regular rectangular domain, $(\xi, \eta) \in [0, 1] \times [0, G]$ as shown in Fig. 3(right). Using the chain rule, the radial and axial derivatives $\frac{\partial}{\partial r}$ and $\frac{\partial}{\partial z}$ are

$$\begin{cases} \dfrac{\partial}{\partial r} = \dfrac{\partial}{\partial \xi} - \eta \dfrac{h'}{h} \dfrac{\partial}{\partial \eta}, \\ \dfrac{\partial}{\partial z} = \dfrac{G}{h} \dfrac{\partial}{\partial \eta}. \end{cases} \tag{10}$$

Incorporating (9) and (10) in (1), the radial and axial velocity components are redefined as

$$U_r = \frac{G}{\xi h} \frac{\partial \psi}{\partial \eta} \ \text{ and } \ U_z = -\frac{1}{\xi} \left(\frac{\partial \psi}{\partial \xi} - \eta \frac{h'}{h} \frac{\partial \psi}{\partial \eta} \right). \tag{11}$$

In a similar way, $\frac{\partial^2}{\partial r^2}$ and $\frac{\partial^2}{\partial z^2}$ are obtained by applying the chain rule twice on (10). We then obtain

$$\begin{cases} \dfrac{\partial^2}{\partial r^2} = \dfrac{\partial^2}{\partial \xi^2} - 2\eta \dfrac{h'}{h} \dfrac{\partial^2}{\partial \xi \partial \eta} + \dfrac{\eta^2 h'^2}{h^2} \dfrac{\partial^2}{\partial \eta^2} + \eta \left(\dfrac{2h'^2 - h''h}{h^2} \right) \dfrac{\partial}{\partial \eta}, \\ \dfrac{\partial^2}{\partial z^2} = \dfrac{G^2}{h^2} \dfrac{\partial^2}{\partial \eta^2}. \end{cases} \tag{12}$$

Here, h'' denotes the free surface second derivative. Incorporating (9), (10), and (12) in (3), (4), and (5) leads to the following new equations of motion:

$$\frac{\partial}{\partial \xi} \left(\frac{G}{\xi h} \frac{\partial \psi}{\partial \eta} \omega \right) - \frac{\partial}{\partial \eta} \left(\frac{G}{\xi h} \frac{\partial \psi}{\partial \xi} \omega \right) + \frac{G h'}{\xi h^2} \frac{\partial \psi}{\partial \eta} \omega - \frac{G}{h} \frac{\partial}{\partial \eta} \left(\frac{\Gamma^2}{\xi^3} \right) - \frac{1}{Re} \left\{ \frac{\partial^2 \omega}{\partial \xi^2} - 2\eta \frac{h'}{h} \frac{\partial^2 \omega}{\partial \xi \partial \eta} \right.$$
$$\left. + \left(\frac{\eta^2 h'^2 + G^2}{h^2} \right) \frac{\partial^2 \omega}{\partial \eta^2} + \frac{1}{\xi} \frac{\partial \omega}{\partial \xi} - \frac{\omega}{\xi^2} + \eta \left(\frac{2h'^2 - h''h}{h^2} - \frac{h'}{\xi h} \right) \frac{\partial \omega}{\partial \eta} \right\} = 0, \tag{13}$$

$$\xi \omega - \frac{\partial^2 \psi}{\partial \xi^2} + 2\eta \frac{h'}{h} \frac{\partial^2 \psi}{\partial \xi \partial \eta} - \left(\frac{\eta^2 h'^2 + G^2}{h^2} \right) \frac{\partial^2 \psi}{\partial \eta^2} + \frac{1}{\xi} \frac{\partial \psi}{\partial \xi} - \eta \left(\frac{2h'^2 - h''h}{h^2} + \frac{h'}{\xi h} \right) \frac{\partial \psi}{\partial \eta} = 0, \tag{14}$$

$$\frac{\partial}{\partial\xi}\left(\frac{G}{h}\frac{\partial\psi}{\partial\eta}\Gamma\right)+\frac{Gh'}{h^2}\frac{\partial\psi}{\partial\eta}\Gamma-\frac{\partial}{\partial\eta}\left(\frac{G}{h}\frac{\partial\psi}{\partial\xi}\Gamma\right)-\frac{\xi}{Re}\left\{\frac{\partial^2\Gamma}{\partial\xi^2}-2\eta\frac{h'}{h}\frac{\partial^2\Gamma}{\partial\xi\partial\eta}+\left(\frac{\eta^2h'^2+G^2}{h^2}\right)\frac{\partial^2\Gamma}{\partial\eta^2}\right.$$

$$\left.-\frac{1}{\xi}\frac{\partial\Gamma}{\partial\xi}+\eta\left(\frac{2h'^2-h''h}{h^2}-\frac{h'}{\xi h}\right)\frac{\partial\Gamma}{\partial\eta}\right\}=0. \quad (15)$$

Applying (9), (10), and (12) to (6) and (7) leads to the new boundary conditions

$$\begin{cases}\eta=0\ :\ \psi=0\,,\ \omega=\dfrac{G}{\xi h}\dfrac{\partial^2\psi}{\partial\eta^2}\ \text{ and }\ \Gamma=\xi^2,\\ \xi=0\ :\ \psi=0\,,\ \omega=0\ \text{ and }\ \Gamma=0,\\ \xi=1\ :\ \psi=0\,,\ \omega=\dfrac{\partial^2\psi}{\partial\xi^2}\ \text{ and }\ \Gamma=0,\\ \eta=G\ :\begin{cases}\psi=0,\\ \xi\omega=\dfrac{-2Gh''h'}{h^2(h'^2+1)}\dfrac{\partial\psi}{\partial\eta},\\ -h'\left(\dfrac{\partial\Gamma}{\partial\xi}-\dfrac{2\Gamma}{\xi}\right)+\dfrac{G(h'^2+1)}{h}\dfrac{\partial\Gamma}{\partial\eta}=0.\end{cases}\end{cases} \quad (16)$$

For the investigation to be described in Sec. II C, we will also need the equations in the primitive form

$$\frac{1}{\xi}\frac{\partial(\xi U_r)}{\partial\xi}-\eta\frac{h'}{h}\frac{\partial U_r}{\partial\eta}+\frac{G}{h}\frac{\partial U_z}{\partial\eta}=0, \quad (17)$$

$$U_r\frac{\partial U_r}{\partial\xi}+\left(\frac{G}{h}U_z-\eta\frac{h'}{h}U_r\right)\frac{\partial U_r}{\partial\eta}-\frac{U_\theta^2}{\xi}=-\frac{\partial\mathcal{P}}{\partial\xi}+\eta\frac{h'}{h}\frac{\partial\mathcal{P}}{\partial\eta}+\frac{1}{Re}\left(\nabla^2U_r-\frac{U_r}{\xi^2}\right), \quad (18)$$

$$U_r\frac{\partial U_\theta}{\partial\xi}+\left(\frac{G}{h}U_z-\eta\frac{h'}{h}U_\theta\right)\frac{\partial U_\theta}{\partial\eta}+\frac{U_rU_\theta}{\xi}=\frac{1}{Re}\left(\nabla^2U_\theta-\frac{U_\theta}{\xi^2}\right), \quad (19)$$

$$U_r\frac{\partial U_z}{\partial\xi}+\left(\frac{G}{h}-\eta\frac{h'}{h}\right)U_z\frac{\partial U_z}{\partial\eta}=-\frac{G}{h}\frac{\partial\mathcal{P}}{\partial\eta}+\frac{1}{Re}\nabla^2U_z, \quad (20)$$

from which we can calculate the pressure. Here,

$$\nabla^2=\frac{\partial^2}{\partial\xi^2}-2\eta\frac{h'}{h}\frac{\partial^2}{\partial\xi\partial\eta}+\left(\frac{\eta^2h'^2+G^2}{h^2}\right)\frac{\partial^2}{\partial\eta^2}+\frac{1}{\xi}\frac{\partial}{\partial\xi}+\eta\left(\frac{2h'^2-h''h}{h^2}-\frac{h'}{\xi h}\right)\frac{\partial}{\partial\eta} \quad (21)$$

denotes the cylindrical Laplacian with curvilinear coordinates. The pressure at the free surface $\mathcal{P}(\xi, G)$ is obtained by integrating $\partial\mathcal{P}/\partial\xi$ between $\xi=0$ to 1. From (18) and (20) we obtain

$$\frac{\partial\mathcal{P}}{\partial\xi}=-U_r\frac{\partial U_r}{\partial\xi}-U_z\frac{\partial U_z}{\partial\xi}+\frac{U_\theta^2}{\xi}+\frac{1}{Re}\left(-h'\left(\frac{\partial\omega}{\partial\xi}+\frac{\omega}{\xi}\right)+\frac{G(h'^2+1)}{h}\frac{\partial\omega}{\partial\eta}\right), \quad (22)$$

where ω is the vorticity defined in (2).

The governing equations (13)–(15) are discretized on an equispaced grid using second-order central differences to approximate all spatial derivatives (see Fig. 3(b)). For a given set of parameters (G and Re), the discretized equations of motion and boundary conditions (13)–(16) are computed using a Newton-Raphson algorithm. A zero velocity field serves as the initial guess. However, in a few cases at larger values of Re, a solution from an intermediate Re value has been used as an initial guess.

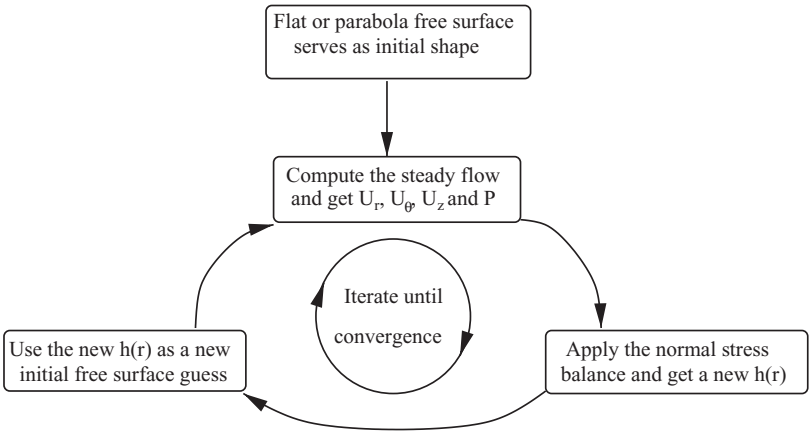

FIG. 4. Schema of the iterative process used to predict simultaneously the free surface shape and the steady state.

C. Free surface shape computation

Equations (13)–(15) describe the flow for a given shape of the interface $h(\xi)$. However, they do not specify the shape $h(r)$ from the two parameters G and Re. In addition to the ordinary unknown variables, the free surface shape $h(\xi)$ is also an unknown that must be found simultaneously with the others. The shape of the interface is well established for solid body rotation since *Newton* studied this phenomena in the 17th century. It is known by the name of *Newton's bucket* for which the free surface takes the shape of an upward-opening circular paraboloid form with the following dimensionless equation:

$$h(r) = G + \frac{Fr}{2}\left(r^2 - \frac{1}{2}\right). \tag{23}$$

Here, $Fr = \Omega^{*2}R^*/g^*$ denotes the Froude number and defines the ratio between the characteristic centrifugal and gravitational accelerations. However, because in our case the vertical side wall is maintained motionless, the free surface shape is not given by Eq. (23). Recall that the free surface is an interface separating the fluid and the ambient air at $z = h(r)$. The steady axisymmetric flow determines the leading-order free surface deflection $h(r)$ under the influence of gravity, pressure and viscous forces. From the balance of the normal stresses $[\mathbf{n} \cdot \sigma \cdot \mathbf{n}] = 0$, we obtain a new free surface deflection

$$\frac{h(r)}{Fr} = \mathcal{P} - \frac{2}{Re(1+h'^2)}\left(h'^2\frac{\partial U_r}{\partial r} + \frac{\partial U_z}{\partial z} - h'\left(\frac{\partial U_r}{\partial z} + \frac{\partial U_z}{\partial r}\right)\right) + c. \tag{24}$$

Here, σ is the stress tensor, $\mathcal{P}$ the pressure along the free surface, and c a constant that ensures volume conservation $\int_0^{2\pi}\int_0^1 h(r)rdrd\theta = \pi G$. Moreover, Eq. (24) must be projected into curvilinear coordinates (ξ, η) leading to

$$\frac{h(\xi)}{Fr} = \mathcal{P} - \frac{2}{Re}\left(\frac{G}{h}\frac{\partial}{\partial\eta}\left(U_z - h'U_r\right) - \frac{h''h'}{(h'^2+1)}U_r\right) + c. \tag{25}$$

Equation (25) relates the radial variation of the interface $h(r)$ to the values of $\mathcal{P}$, U_r, U_z, h', and h'' at the interface ($\eta = G$). At the same time, the equations of motion (13)–(15) and boundary conditions (16) involve the interface shape (h, h', and h''). The coupled equations of motion (13)–(16) and the free surface radial deflection (25) can be satisfied simultaneously via an iterative process. Fig. 4 illustrates this iterative process. We start by fixing G, Re, Fr and an initial shape of the free surface $h(r)$, for example, flat ($h(r) = G$) or parabolic (23) for the case of large deflection. Then we compute the steady axisymmetric base flow via (13)–(16) in order to obtain the values of U_r, U_θ, U_z, and $\mathcal{P}$ at the free surface. The pressure at the interface $\mathcal{P}(\xi, G)$ is obtained by integrating (22) between $\xi = 0$ and 1. Applying the normal stress balance (25) leads to the first interface deflection $h(r)$, which can

be used as a new guess to compute again the steady axisymmetric base flow (13)-(16), and obtain new values of U_r, U_θ, U_z, and $\mathcal{P}$ which correspond to the new interface deflection. Finally, we iterate until convergence so as to obtain the velocity field **U** with the adequate free surface deformation $h(r)$. The hypothesis of a flat and fixed free surface is equivalent to $Fr = 0$, for which the iterative process illustrated in Fig. 4 is useless. Weak free surface deformation is equivalent to a small value of Froude number and only three or four iterations are required to obtain the velocity field **U** with the adequate free surface deformation $h(r)$.

However, for a strong free surface deformation, the iterative process will fail if no special care is taken. A relaxation factor $\alpha \in]0, 1[$ is required with the following relation:

$$h_{new} = (1 - \alpha)h_{old} + \alpha\hat{h}_{new}, \tag{26}$$

where $\hat{h}_{\text{new}}$ is the left-hand side of (25), all terms on the right-hand side are evaluated at the previous iteration. The present formulation assumes that the normal **n** is defined for any point on the free surface. This is a limitation of the method that would not be able to capture a free surface shape with sharp cusps for instance. Depending on the configuration, the convergence has not been achieved to machine precision. In such case, the residual defined as the L2 norm of $h_{\text{new}} - h_{\text{old}}$ then reaches a minimum value and eventually diverges. We stopped the iterative process at the minimum value. A closer inspection of the free surface deflection reveals that the increase of the L2 norm leading to divergence is due to formation of a sharp cusp that is incompatible with the present numerical method. However, as discussed in Sec. III, the cusp may have a physical ground but is likely to be smoothed locally by surface tension in the experiment. In the results of Herrada *et al.*,[20] in which surface tension effects are large, no such cusp is observed. Investigations on the effect of surface tension as well as wettability on the periphery is beyond the scope of the present study.

D. Flow description for the case of flat free surface and unit aspect ratio

The steady state for $G = 1$ is shown in Fig. 5. We choose to start with unity aspect ratio in order to explain the physical structure of the flow and also to validate our results with previous studies. When the rotating disk is in motion, a centrifugal Ekman boundary layer[21] develops above it making the fluid spiral out toward its periphery. This spiral motion reaches the fixed vertical side wall, inducing a second boundary layer, called the Stewartson layer,[22] in its vicinity. The motion reaches the free surface and then decelerates toward the z-axis by a centripetal spiral motion. Under the Ekman pumping effect, the fluid returns to the rotating disk by a swirling motion around the z-axis. For specific values of Re, one or several stagnation points occur in the $r - z$ plane developing a secondary toroidal circulation. For enclosed cavities, i.e., a rotor-stator configuration, these secondary circulations appear only on the z-axis. However, the free surface allows their development on both z-axis and the free surface (see Figure 5 which is related to ψ). Spohn[1] provided a $G - Re$ map of the appearance of secondary circulations. At $Re = 450$, no secondary circulation appears. Increasing Re to 460, slight secondary toroidal circulation, with very low intensity, develops at the z-axis. This was already detected numerically by Daube[4] but not experimentally by Spohn.[1] At $Re = 900$, a secondary circulation is located at the top of the z-axis. This was observed experimentally by Spohn[1] and detected numerically by Piva and Meiburg[6] and Bouffanais and Jacono.[23] At $Re = 1120$, the secondary toroidal circulation detaches from the z-axis. Piva and Meiburg[6] provided a very clean experimental observation of this situation. Finally, $Re = 1500$ induces an off-axis secondary circulation attached only at the free surface. Our computations show a reasonable agreement with previous studies. However, depending on the chosen criterion, the agreement can be fair to poor. For instance, for $Re = 900$, the comparison of the extremum values of ψ and U_z shows a good agreement with Piva and Meiburg[6] as we found 0.010, -2.11×10^{-4}, 0.122, and -0.084 for ψ_{max}, ψ_{min}, $U_{z_{max}}$, and $U_{z_{min}}$, respectively. Focusing on the stagnation point at the z-axis ($U_z = 0$ at $r = 0$), some discrepancies are found. The stagnation point is located at $z \sim 0.41$, a value close to the one found by Bouffanais and Jacono[23] ($z \sim 0.39$) but differs from the value $z \sim 0.3$ of Piva and Meiburg.[6] For $Re = 800$ (not represented here), the comparison is satisfactory with Daube[4] as we both found $z \sim 0.35$.

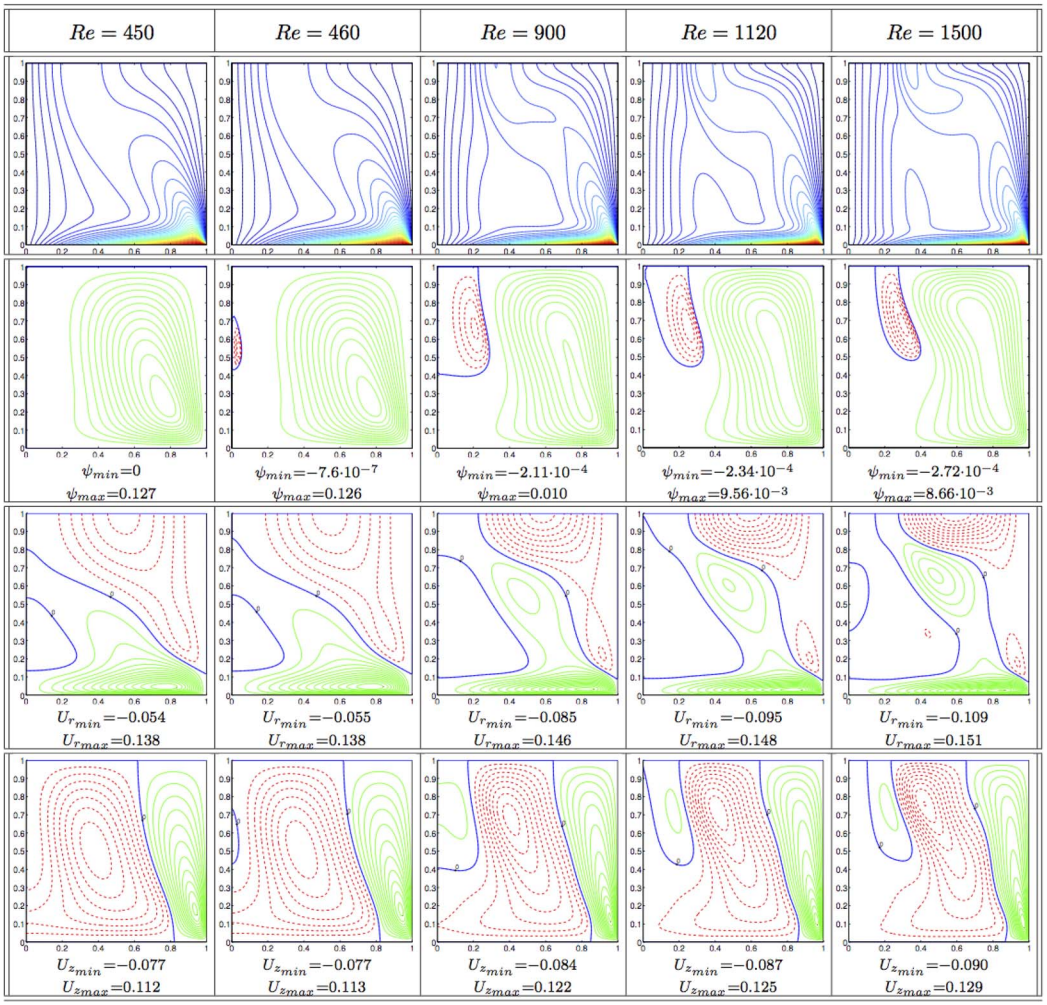

FIG. 5. From top to bottom, steady flow contours of U_θ, ψ, U_r, and U_z, respectively, in a unity aspect ratio. Solid (dashed) lines refer to positive (negative) values. The spatial resolution is $N_r \times N_z = 151^2$. The contours are equally spaced with steps of 0.05 for U_θ and 0.01 for U_r, and U_z. The ψ contours are given with a step of 0.001 (5×10^{-5}) for positive (negative) contours except for $Re = 460$ where the negative contours are given with step 10^{-7}.

III. RESULTS

In this section, we start by summarizing the global flow shape for the situation of small aspect ratio and assuming a flat free surface (Sec. III A). We focus further on the evolution of the flow structures in the r-z plane which are secondary cell vortices. Section III B describes the free surface shape for cavities of unit aspect ratios and shows a quantitative comparison with previous studies (Piva and Meiburg[6] and Bouffanais and Lo Jacono[17]). Finally, Sec. III C presents an experimental setup for free surface deflection measurements which are compared to the numerical simulation.

A. Meridional secondary cells for very small aspect ratio

The cavities whose aspect ratio G varies between 0.25 and 4 have been studied by Refs. 4, 6, 7, and 23–26. For values of $G \ll 1$ and Re close to the linear stability threshold Re_c (see Kahouadji *et al.*[27]), the shape of the base flow is similar to that in Fig. 6 which shows, respectively, from top to bottom, the azimuthal velocity field U_θ, radial U_r, and axial U_z velocity fields. The corresponding streamlines shape is shown in the bottom of Fig. 7. This figure shows that, close to the z-axis, the fluid motion rotates as a solid body rotation with the angular velocity of the disk. This can be seen

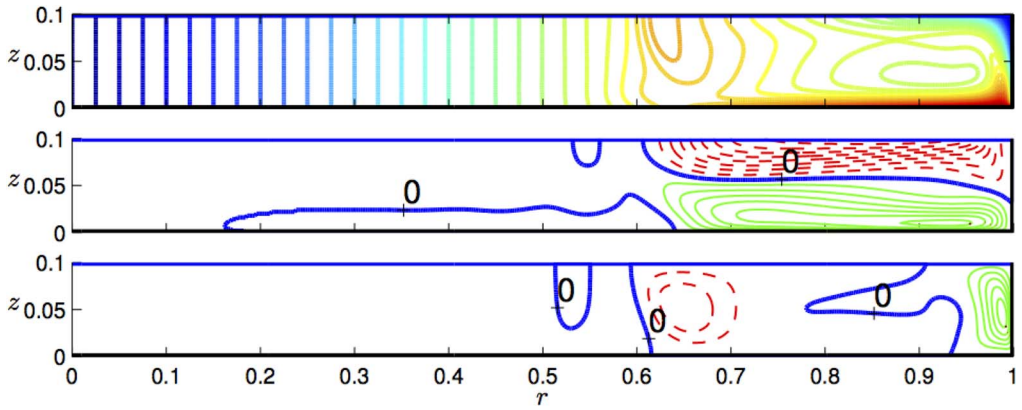

FIG. 6. Steady flow contours, from top to bottom, of U_θ, U_r, and U_z for $G = 0.1$ and $Re = 10\,000$. The contours are equally spaced with steps of 0.05 for U_θ and 0.02 for U_r, and U_z. See Fig. 7 bottom for the associated streamline contours.

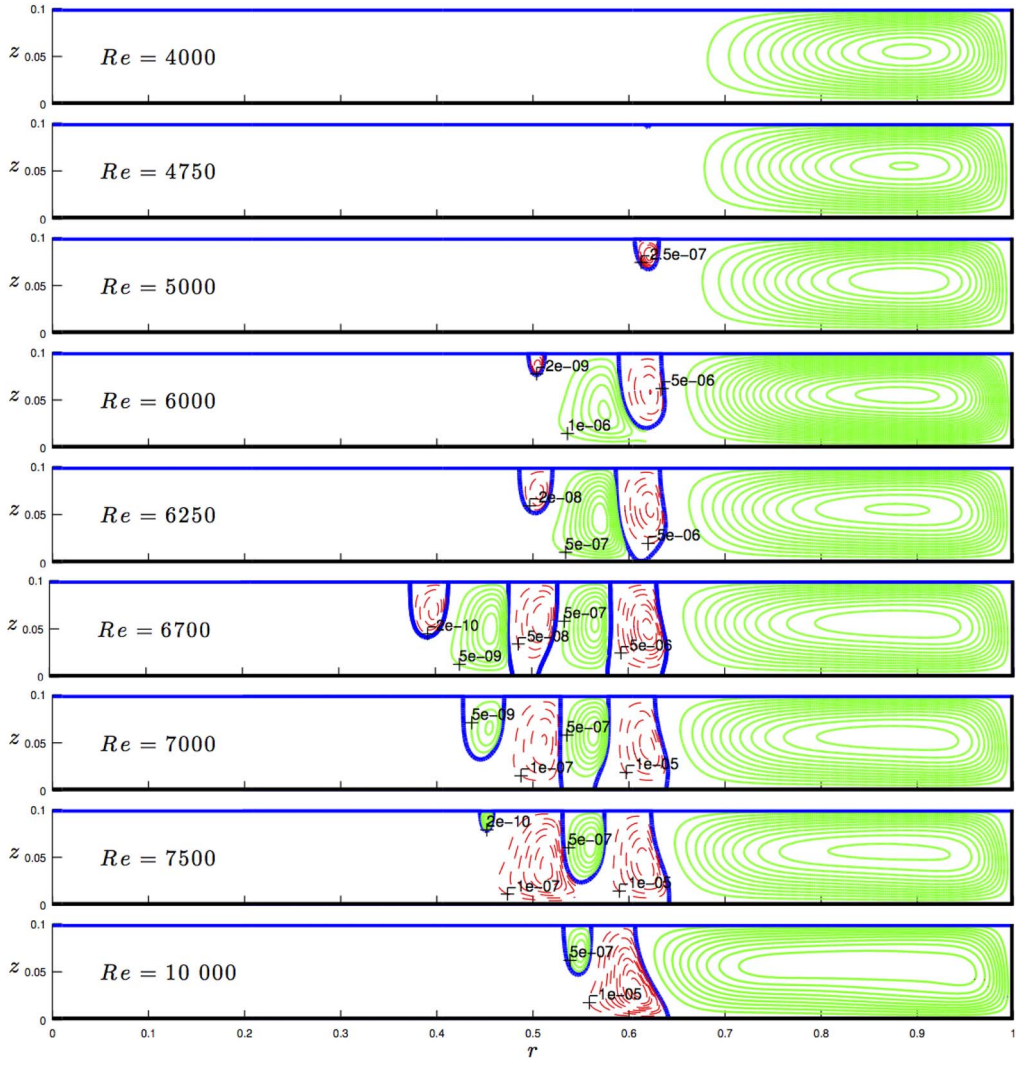

FIG. 7. Streamline contours for $G = 0.1$ and Re varying between 4×10^3 and 10^4. The spatial resolution is $N_r \times N_z = 501 \times 51$. The contours of the principal recirculation are uniformly spaced with the step 0.003. For each eddy structure, the contours are also uniformly spaced. The chosen step for each eddy is specified directly in the figure.

precisely with the contours of U_θ which are vertical lines and uniformly spaced in the radial direction ($U_\theta \sim r$) and leading to zero values of U_r and U_z (and thus of ψ). This area with solid body rotation extends radially when G is smaller. Such behavior has been observed numerically by Kahouadji,[28] Herrero *et al.*,[29] and Randriamampianina *et al.*[30] for a configuration of an enclosed corotating disk pair. Beyond this solid body rotation area, the fluid motion resembles with that described for $G = 1$ forming a secondary toroidal circulation. Moreover, several stagnation points occur, between the solid body rotation area and the primary meridional circulation near the fixed side wall, forming two other secondary circulation cells (Fig. 7 (bottom)).

For $G = 0.1$, Kahouadji *et al.*[27] found the critical Reynolds number for breaking axisymmetry with an azimuthal mode 4 approximately equal to 11 000 which is in reasonable agreement with the value found experimentally by Poncet and Chauve.[8] Fig. 7 shows, for fixed $G = 0.1$, the evolution of meridional flow structures for several values of Re. Starting with $Re = 4000$, the flow structure in the r-z plan is composed only of a principal circulation (PC^+) due to the fixed vertical side wall that we already described in Sec. II D. We use the notations $^{(+)}$ and $^{(-)}$ corresponding to the signs of the stream-function for each structure, i.e., the circulation is directed anti-clockwise for $^{(+)}$ and clockwise for $^{(-)}$. At $Re \sim 4750$, a very small secondary cell SC_1^-, attached to the free surface, starts to appear at $r \sim 0.62$ and grows when the Reynolds number is increased (see the case $Re \sim 5000$ in Fig. 7). When $Re \sim 6000$, SC_1^- grows further and generates another secondary cell SC_2^+ at $r \sim 0.57$. Also at the same Re, a new cell SC_3^- appears at the free surface at $r \sim 0.5$, turning in the same direction as SC_1^-. At $Re \sim 6250$, the secondary cells SC_1^-, SC_2^+, and SV_3^- grow further in volume and also in intensity. We notice that SC_1^- and SC_2^+ occupy the entire fluid height (i.e., from the free surface to the rotating disk). At $Re \sim 6700$, there are a multitude of secondary cells SC_1^-, SC_2^+, SC_3^-, SC_4^+ (at $r \sim 0.45$) and SC_5^- (at $r \sim 0.4$). This is the situation in which we attained the maximum number of secondary cells. Increasing Re until 7000, we notice that SC_5^- disappears. At $Re = 7500$, SC_4^+ becomes smaller before vanishing at the free surface. Finally at $Re \sim 10\,000$, SC_3^+ disappears completely, leaving only SC_1^-, next to PC^+ at $r \sim 0.6$, and a very small $SC_2^{(+)}$ attached to the free surface at $r \sim 0.55$.

This multitude of such secondary cells are also detected for $G = 0.05$. Fig. 8 shows the evolution of flow structures in the r-z plane as a function of Re. For $Re < 17\,250$, the fluid rotates as a solid body rotation (for $0 < r < 0.75$). It is only near the fixed vertical side wall ($0.75 < r < 1$) that we obtain a principal circulation PC^+. At $Re \sim 17\,300$, a very small SC_1^- attached to the free surface appears at $r \sim 0.72$ which also amplifies when Re is increased (for example, $Re = 19\,000$). At $Re \sim 20\,000$, SC_1^- occupies the entire fluid height and reaches the rotating disk and then generates, by viscous effects, SC_2^+ at $r \sim 0.7$. Further increasing Re, it generates other secondary vortices for which we reach the maximum number at $Re = 21\,500$ (SC_1^-, SC_2^+, SC_3^-, SC_4^+, SC_5^-, and SC_6^+). Beyond this value, most of the secondary vortices disappear one by one, leaving only SC_1^- confined to PC^+ and SC_2^+.

Similar secondary cells have been observed for larger aspect ratio. Brøns *et al.*[5] found a sequence of four cells for $G = 0.3$ and $Re = 2100$. Iwatsu[31] for $G = 0.3$ and $Re = 1000$ observed one cell attached to the free surface. Hewitt *et al.*[32] observed experimentally, for the case of an enclosed co-rotating disks, several secondary cells attached to the horizontal mid-plane that could be assimilated to our free surface using an axial reflectional symmetry. Finally, Bouffanais and Lo Jacono[23] observed four cells for $G = 1/3$ and $Re = 2000$.

B. Deformable free surface

This section treats the interface deflection for both weak and strong deformations. Fig. 9(a) shows the relative interface deflection $\frac{h(r)-G}{Fr}$ as a function of the radius r. The Froude number varies between 0.1 and 1. For each Reynolds number (900 and 1500), the curves for different Froude numbers are very close. It is only by magnifying near the axis that we perceive the existence of a tiny variation of $\frac{h(r)-G}{Fr}$ as a function of Fr. The experimental study of Suzuki *et al.*[11] measured the interface height at the axis as a function of Re. As long as the interface does not reach the rotating disk, $h(0)$ decreases monotonically as a function of Re. By representing $h(0) - G$ as a function of Fr,

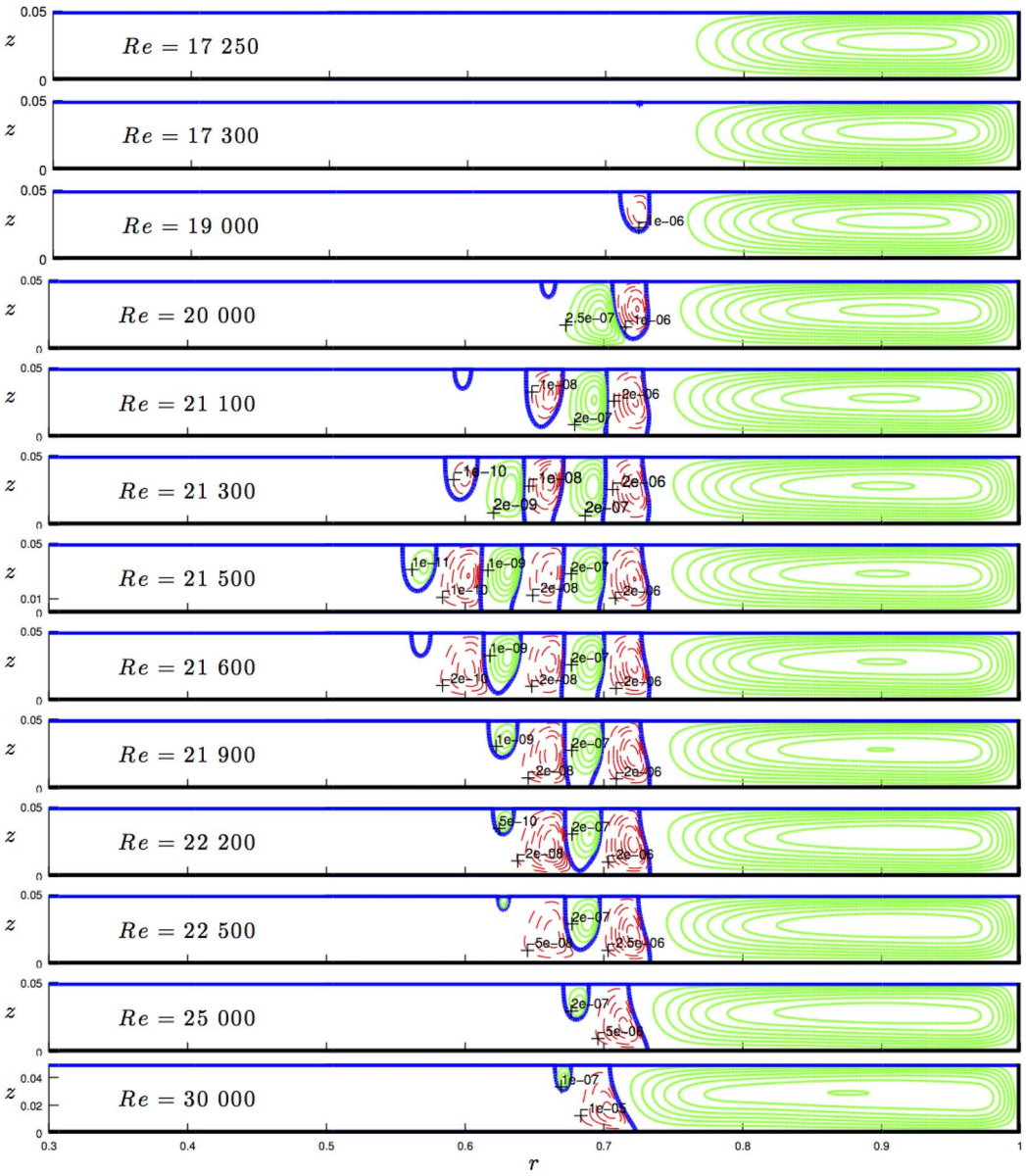

FIG. 8. Streamline contours for $G = 0.05$ and Re varying between 1.725×10^4 and 3×10^4. The spatial resolution is $N_r \times N_z = 1001 \times 51$. The contours of the principal recirculation are uniformly spaced with the step 0.002. For each eddy structure, the contours are also uniformly spaced. The chosen step for each eddy is specified directly in the figure.

instead of Re, we obtain a linear decreasing as it is shown in Fig. 9(b). This linear variation can be explained by the Newton Bucket formula (23) because, near the axis, the flow behaves almost as a solid rotating body even with the existence of a secondary cells. This explains why the interface near the axis has the shape of a concave parabola which Vatistas[9] described as an inverted bell. Moreover, if we consider the same experiment, with the same fluid, the Froude number can be written as a function of Reynolds number via $Fr = Re^2/Ga$, where $Ga = \frac{g^* R^{*3}}{\nu^{*2}}$ is a constant dimensionless value, for the same experiment and the same fluid, which is called the Galileo number. Consequently, the interface deflection $h(0) - G$ decreases parabolically as a function of Re.

In Table I, we report the values of $|\frac{h(0)-G}{Fr}|$ deduced from Figure 3(a) of Bouffanais and Lo Jacono[17] and Figure 14 of Piva and Meiburg.[6] For $Re = 900$, there is a quantitative disagreement in the interface depth at the z-axis. Our values are close to the computations of Piva and Meiburg.[6]

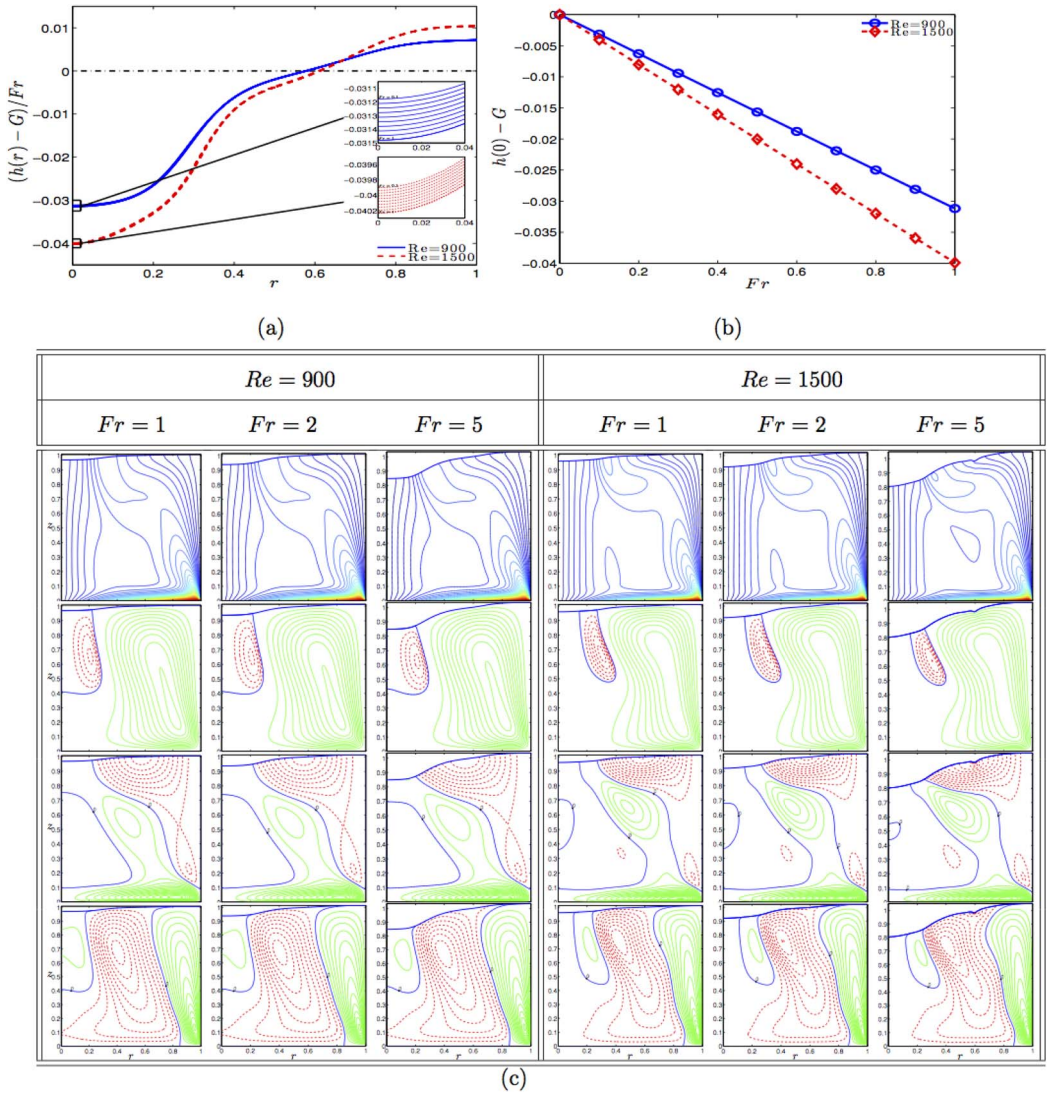

FIG. 9. $N_\xi \times N_\eta = 151^2$, $G = 1$, $Re = 900$ and 1500. (a) Relative free surface deflection $(h(r) - G)/Fr$. The magnifications show the weak influence of Froude in the range of $0.1 \leq Fr \leq 1$. (b) Free surface deflection at the z-axis $(h(0) - G)$ as a function of Fr. (c) Steady contours of U_θ (with step 0.05), ψ (with step of 0.001 for positive values and 5×10^{-5} for negative values), U_r and U_z (with step 0.01), respectively.

The slight disagreement can be explained by the fact that their calculations also use a zero normal stress at the interface, for which the velocity field at the interface is deduced from a flat free surface model (i.e., the first-order approximation of the deflection). In our calculation with the curvilinear coordinate projection and the iterative process, the velocity field also takes into account surface deflection. In fact, the first-order approximation simply corresponds to the first iteration of the

TABLE I. For $G = 1$ and $Fr = 0.1$, relative interface deflection $|\frac{h(0)-G}{Fr}|$ at the axis.

Re	Bouffanais and Jacono[17]	Piva and Meiburg[6]	Our calculation
900	$\sim 6.7 \times 10^{-2}$	$\sim 3 \times 10^{-2}$	3.2×10^{-2}
1500	$\sim 8.5 \times 10^{-2}$	No value	4.1×10^{-2}

iterative process with a relaxation factor $\alpha = 1$. In contrast, the values of Bouffanais and Lo Jacono[17] are twice as large as ours even with a very small Froude number ($Fr = 0.1$). Furthermore, the disagreement is not only in the values of $|\frac{h(0)-G}{Fr}|$ but also about the global shape of the free surface as a function of the radius r (see Figure 3(a) of Bouffanais and Lo Jacono[17]). From Figs. 9(a) and 9(c), the shape of the free surface near the axis remains close to a parabola regardless of the values of Re (900 or 1500) or Fr (between 0.1 and 5). Both Suzuki *et al.*,[11] Vatistas,[9] and Piva (private communication) experimentally observed a concave parabolic shape with a minimum at the z-axis but Bouffanais and Lo Jacono[17] observed a local maximum at the z-axis for $Re = 900$.

Even though we obtain a qualitative agreement with the interface shape in the experimental studies by Suzuki *et al.*,[11] Tasaka *et al.*,[14] and Vatistas,[9] we should compare our numerical calculations with experimental measurements in order to better validate our computational results. For this reason, Sec. III C is dedicated to presenting an experimental setup for measuring interface deflections.

C. Comparison between numerical calculations and experimental measurements

Fig. 10(a) shows the experimental setup, consisting of a transparent plexiglas cylinder with an inner radius $R^* = 62.5$ mm fixed on a heavy circular metallic support. The rotating disk of radius R^* located at the bottom of the cylinder is connected at its center to a bevel gearbox which serves to convert the horizontal rotating motion of an electric motor to the vertical rotating motion. We use car engine oil with a density of $\rho^* \sim 866$ kg m^{-3} and dynamic viscosity $\mu^* \sim 49.5 \times 10^{-3}$ Pa s. This choice of oil maintains laminar flow even under significant free surface deformation. A vertical needle connected to a mechanism which slides horizontally and vertically above the cavity is used for measuring the free surface height as a function of the radius. With the appropriate lighting, the

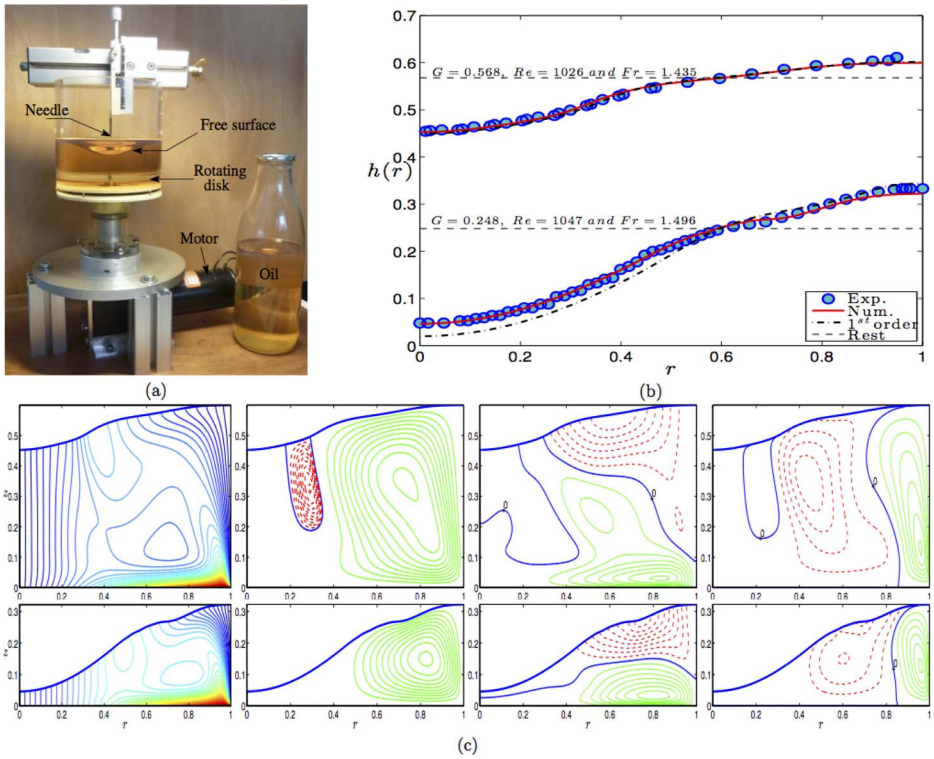

FIG. 10. (a) Experimental photograph describing the way in which the free surface deflection is measured by a vertical needle. (b) A superposition of the experimental measurements, first-order approximation, and the numerical results of a free surface deflection for (G, Re, Fr) = (0.568, 1026, 1.435) and (0.248, 1047, 1.496) and (c) numerical flow contours of U_θ (with step 0.05), ψ (with step 0.01 for positive values and 2×10^{-5} for negative values), U_r and U_z (with step 0.02) from left to right, respectively.

needle reflects on the free surface acting like a mirror. The needle is moved vertically toward the free surface and stopped as it almost touches its image. An *a posteriori* validation by computing the global volume with trapezoidal integration of the measured height is done. The value differed by less than 1% of that of the initial volume in the facility even for deflection comparable to the initial height at rest. This apparatus cannot be used for small values of Fr and for aspect ratios G larger than 0.6. We estimate the accuracy to be around 0.5 mm. For the radius of our experiment, the values in Table I would correspond to a total deflection of 0.2 mm for $Re = 900$ and 0.26 mm for $Re = 1500$ and cannot be measured. However, large deflection, which are much more computationally challenging for the curvilinear coordinate projection, is well fitted for the experimental setup. The measurements presented in Fig. 10(b) correspond to the two following set of parameters:

1. Angular velocity $\Omega_1^* = 15.0$ rad/s and fluid height at rest $H_1^* = 35.5$ mm.
2. Angular velocity $\Omega_2^* = 15.3$ rad/s and fluid height at rest $H_2^* = 15.5$ mm.

These two configurations correspond to the following dimensionless control parameters $(Re_1, Fr_1, G_1) = (1026, 1.435, 0.568)$ and $(Re_2, Fr_2, G_2) = (1047, 1.496, 0.248)$. The flow structure is shown in Fig. 10(c). The experimental measurements and the numerical calculation, shown in Fig. 10(b), agree quantitatively for the two curves. The experimental and the numerical interface deflection at the z-axis are -7.1 mm and -7.2 mm, respectively, for the experimental set (Re_1, Fr_1, G_1) and -12.5 mm and -12.6 mm, respectively, for the experimental set (Re_2, Fr_2, G_2). The curvilinear coordinate projection with the iterative process used in this study seems appropriate even for large deflection. If the calculations are valid for these two examples, corresponding to a moderate Froude number Fr_1 and Fr_2, they are likely to be valid for smaller Fr and match the first-order approximation. The free surface shape presented in Fig. 9(a) is indeed quite close to the one presented by Piva and Meiburg[6] (within a few percent). Even for larger deflection, such as the shapes presented in Fig. 10(b), the first-order approximation compares surprisingly well with the numerical computation (and experiment). For the experimental set 1, numerical (solid line) and first-order approximation (dashed-dotted line) cannot be distinguished in Fig. 10(b) and for the experimental set 2, the deflection at the z-axis is overestimated by 13.5%.

The shape of the free surface deflection is better understood if one analyzes each contribution in (25) for the computation of $h(r)$. As an illustration, we choose the set 2 which is the most challenging from a numerical point of view and exhibits the main features of the regimes studied in this section. The Reynolds value is large enough so that the contribution of the viscous terms in the normal stresses balance (25) is small compared to pressure. The latter is obtained by integrating (22). In this equation, the convective terms (first three terms of the right-hand side) dominate over viscous terms. Out of these terms, the contribution due to azimuthal velocity $\frac{U_\theta^2}{\xi}$ is dominant over the two meridional terms $-U_r \frac{\partial U_r}{\partial \xi}$ and $-U_z \frac{\partial U_z}{\partial \xi}$. Artificially removing all terms except $\frac{U_\theta^2}{\xi}$ and pressure in the right-hand side of (22) and (25), respectively, leads roughly to the shape presented in Fig. 10(b). If the two meridional convective terms are added the actual shape is close to be recovered. Thus, the azimuthal contribution U_θ^2/ξ at the free surface, presented in Fig. 11 allows to understand the shape. For $0 < r \lesssim 0.45$, the solid body rotation leads to a parabola that corresponds to a Newton's bucket with half radius, rotating at the same angular velocity but initially filled with less fluid. The volume over this central region decreased as part of the fluid has been expelled toward the periphery during the spin up. For these specific parameters, the volume in the parabola region loses approximately half of its initial volume at rest. For $r \gtrsim 0.5$, the azimuthal velocity decreases to satisfy the boundary condition at the fixed side wall and thus the slope of $h(r)$ decreases. The volume transferred from the central uniformly rotating region is less than what would be expected if the side wall was also rotating. In such case, most of the central region would be dewetted.

A second observation is a smooth cusp-like shape at $r \sim 0.7$. This is due to the meridional convective terms and more specifically to $-U_r \frac{\partial U_r}{\partial \xi}$ represented in Fig. 11. The other meridional contribution (not represented) $-U_z \frac{\partial U_z}{\partial \xi}$ is smaller. This meridional term is comparable to the azimuthal contribution in the cusp region and more importantly cancels at $r \sim 0.75$ which leads to a local minimum of pressure and consequently a local minimum of the free surface height. From Fig. 10(c), it can be noted that the magnitude of the radial velocity along the free surface is maximum

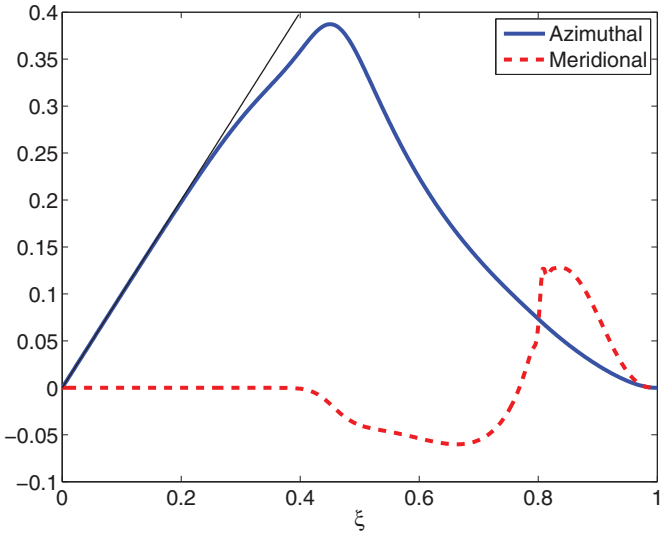

FIG. 11. The two main contributions in the computation of the radial pressure gradient (22) plotted at the free surface as a function of ξ. Solid blue line: Azimuthal contribution $\frac{U_\theta^2}{\xi}$ and red dashed line: part of the meridional contribution $-U_r \frac{\partial U_r}{\partial \xi}$.

in the same region. The extra path for the radial inward fluid generated by the local minimum in the free surface will decrease locally the pressure and then tends to amplify the cusp. Surface tension will balance this effect.

IV. CONCLUSION

This article has thoroughly investigated a steady flat and deformable free surface in a flow driven by a rotating disk inside a fixed cylindrical tank. For the flat free surface, several secondary vortices were detected. For a deformable free surface, we used curvilinear coordinates associated with an iterative process to simultaneously solve the equations of motions and the zero normal stress condition in order to provide an accurate free surface shape. Two experimental measurements are also presented in order to validate our calculations. This paper gives rise to at least two perspectives. First, one wishes to study the impact of the free surface deflection on the threshold for the flow instability. Second, a better understanding of the mechanism of birth and death of the secondary cells would be interesting. Some explanations can be found in Hewitt *et al.*[32] but it still remains unexplained that the number of cells is not necessarily a monotonous function of *Re* or *G*.

ACKNOWLEDGMENTS

L. Kahouadji acknowledges the warm hospitality of LIMSI-CNRS, in particular J. Chergui, D. Juric, M. Firdaouss, N. Perinet, J. Peixinho, and L. Tuckerman for helpful discussions. L. Martin Witkowski is grateful to S. Poncet and M. Piva for providing experimental data, and C. Nore and W. Herreman for interesting suggestions. We also wish to thank with gratitude E. Pelissier who carefully carried out the experiments described in Sec. III C during an internship at LIMSI-CNRS. We also like to sincerely thank P. Desroches, D. Caqueret, V. Gautier, Y. Maire, and V. Bourdin for their kindhearted help in setting up the experiment shown in Fig. 10(a). Finally, L. Kahouadji also acknowledges financial support from Université Paris-Dauphine and Paris-Descartes.

[1] A. Spohn, and O. Daube, "Recirculating flows in a cylindrical tank," in *Proceedings of the V International Conference on Computational Methods and Experimental Measurement*, edited by A. Sousa, C. A. Brebbia, and G. M. Carlomagno (Elsevier, Montreal, 1991), pp. 155–166.
[2] A. Spohn, M. Mory, and E. Hopfinger, "Observations of vortex breakdown in an open cylindrical container with a rotating bottom," Exp. Fluids **14**, 70–77 (1993).

[3] A. Spohn, M. Mory, and E. Hopfinger, "Experiments on vortex breakdown in a confined flow generated by a rotating disc," J. Fluid Mech. **370**, 73–99 (1998).
[4] O. Daube, "Numerical simulation of axisymmetric vortex breakdown in a closed cylinder," in *Vortex Dynamics and Vortex Methods*, Lectures in Applied Mathematics Vol. 28, edited by C. R. Anderson and C. Greengard (American Mathematical Society, 1991), pp. 131–152.
[5] M. Brøns, L. Voigt, and J. Sørensen, "Topology of vortex breakdown bubbles in a cylinder with a rotating bottom and a free surface," J. Fluid Mech. **428**, 133–148 (2001).
[6] M. Piva and E. Meiburg, "Steady axisymmetric flow in an open cylindrical container with a partially rotating bottom wall," Phys. Fluids **17**, 063603 (2005).
[7] E. Serre and P. Bontoux, "Vortex breakdown in a cylinder with a rotating bottom and a flat stress-free surface," Int. J. Heat Fluid Flow **28**, 229–248 (2007).
[8] S. Poncet and M. Chauve, "Shear-layer instability in a rotating system," J. Flow Visual. Image Process. **14**, 85–105 (2007).
[9] G. H. Vatistas, "A note on liquid vortex sloshing and Kelvin's equilibria," J. Fluid Mech. **217**, 241–248 (1990).
[10] G. H. Vatistas, J. Wang, and S. Lin, "Experiments on waves induced in the hollow core of vortices," Exp. Fluids **13**, 377–385 (1992).
[11] T. Suzuki, M. Iima, and Y. Hayase, "Surface switching of rotating fluid in a cylinder," Phys. Fluids **18**, 101701 (2006).
[12] T. R. N. Jansson, M. P. Haspang, K. H. Jensen, P. Hersen, and T. Bohr, "Polygons on a rotating fluid surface," Phys. Rev. Lett. **96**, 174502 (2006).
[13] A. Abderrahmane, K. Siddiqui, and G. Vatistas, "Transition between Kelvin's equilibria," Phys. Rev. E **80**, 066305 (2009).
[14] Y. Tasaka and M. Iima, "Flow transitions in the surface switching of rotating fluid," J. Fluid Mech. **636**, 475–484 (2009).
[15] R. Bergmann, L. Tophøj, T. A. M. Homan, P. Hersen, A. Andersen, and T. Bohr, "Polygon formation and surface flow on a rotating fluid surface," J. Fluid Mech. **679**, 415–431 (2011).
[16] L. Tophøj, J. Mougel, T. Bohr, and D. Fabre, "Rotating polygon instability of a swirling free surface flow," Phys. Rev. Lett. **110**, 194502 (2013).
[17] R. Bouffanais and D. Lo Jacono, "Unsteady transitional swirling flow in the presence of a moving free surface," Phys. Fluids **21**, 064107 (2009).
[18] P. T. Brady, M. Herrmann, and J. M. Lopez, "Two-fluid confined flow in a cylinder driven by a rotating endwall," Phys. Rev. E **85**, 016308 (2012).
[19] P. T. Brady, M. Herrmann, and J. M. Lopez, "Addendum to "two-fluid confined flow in a cylinder driven by a rotating endwall"," Phys. Rev. E **85**, 067301 (2012).
[20] M. Herrada, V. Shtern, and J. Lopez-Herrera, "Off-axis vortex breakdown in a shallow whirlpool," Phys. Rev. E **87**, 063016 (2013).
[21] V. W. Ekman, "On the influence of the Earth's rotation on the ocean-currents," Arkiv. Mat. Astr. Fys. **2**, 1–52 (1905).
[22] K. Stewartson, "On the flow between two rotating coaxial disks," Proc. Camb. Philos. Soc. **49**, 333–341 (1953).
[23] R. Bouffanais and D. Lo Jacono, "Transitional cylindrical swirling flow in presence of a flat free surface," Comput. Fluids **38**, 1651–1673 (2009).
[24] J. M. Lopez, "Unsteady swirling flow in an enclosed cylinder with reflectional symmetry," Phys. Fluids **7**, 2700–2714 (1995).
[25] J. M. Lopez, F. Marques, A. H. Hirsa, and R. Miraghaie, "Symmetry breaking in free-surface cylinder flows," J. Fluid Mech. **502**, 99–126 (2004).
[26] S. J. Cogan, K. Ryan, and G. J. Sheard, "Symmetry breaking and instability mechanisms in medium depth torsionally open cylinder flows," J. Fluid Mech. **672**, 521–544 (2011).
[27] L. Kahouadji, L. M. Witkowski, and P. Le Quéré, "Seuils de stabilité pour un écoulement à surface libre engendré dans une cavité cylindrique tournante à petit rapport de forme," Méc. Ind. **11**, 339–344 (2010).
[28] L. Kahouadji, "Analyse de stabilité linéaire d'écoulements tournants en présence de surface libre," Ph.D. thesis, Université Pierre et Marie Curie, Paris, France, 2011.
[29] J. Herrero, F. Giralt, and J. Humphrey, "Influence of the geometry on the structure of the flow between a pair of corotating disks," Phys. Fluids **11**, 88–96 (1999).
[30] A. Randriamampianina, R. Schiestel, and M. Wilson, "Spatio-temporal behaviour in an enclosed corotating disk pair," J. Fluid Mech. **434**, 39–64 (2001).
[31] R. Iwatsu, "Analysis of flows in a cylindrical container with rotating bottom and top underformable free surface," JSME Int. J. **47**, 549–556 (2004).
[32] R. Hewitt, T. Mullin, S. Tavener, M. Khan, and P. Treacher, "Nonlinear vortex development in rotating flows," Philos. Trans. R. Soc. A **366**, 1317–1329 (2008).